Article:

Elsakka, M.M., Ingham, D.B. orcid.org/0000-0002-4633-0852, Ma, L. orcid.org/0000-0002-3731-8464 et al. (1 more author) (2021) Comparison of the computational fluid dynamics predictions of vertical axis wind turbine performance against detailed pressure measurements. International Journal of Renewable Energy Research, 11 (1). pp. 276-293.

eprints@whiterose.ac.uk
https://eprints.whiterose.ac.uk/

Comparison of the Computational Fluid Dynamics Predictions of Vertical Axis Wind Turbine Performance Against Detailed Pressure Measurements

Mohamed M. Elsakka[*‡], Derek B. Ingham[**], Lin Ma[***], and Mohamed Pourkashanian[****]

*Mechanical Power Dept., Faculty of Engineering, Port Said University, Egypt

** Energy2050, Faculty of Engineering, University of Sheffield, UK

*** Energy2050, Faculty of Engineering, University of Sheffield, UK

**** Energy2050, Faculty of Engineering, University of Sheffield, UK

(elsakka@eng.psu.edu.eg, d.ingham@sheffield.ac.uk, lin.ma@sheffield.ac.uk, m.pourkashanian@sheffield.ac.uk)

‡ Corresponding Author; 42526, Port Said, Egypt, Tel: + 020 66 340 3459, Fax: +020 66 340 0936, elsakka@eng.psu.edu.eg

Abstract- Computational Fluid Dynamics (CFD) simulations are currently one of the most popular methods for the modelling of a Vertical Axis Wind Turbine (VAWT) that gives good insight on the turbine aerodynamics. The current study provides an assessment of the quality of the 2D and 3D CFD predictions of two highly recommended models in the literature, namely the SST K-ω model and the SST K-ω with the γ Intermittency transition model. The novelty of the study is in the kind of data that is used in the assessment. The CFD predictions of the pressure around the blade at several azimuthal angles are compared to the published experimental data measured by a high-frequency multiport pressure scanner. In addition, the predictions of the pressure contribution to the instantaneous power coefficient are compared to the experimental data. This paper sheds much new light on how the behaviour of the predictions of the SST K-ω with the γ intermittency transition model changes between the 2D and 3D cases and how the trends of the 2D results based on this transition model deviate from the detailed experimental data. This behaviour has not been previously investigated.

Keywords VAWT, CFD, Pressure distribution, Turbulence modelling, Transition.

1. Introduction

In a world of increasing population, the global energy demand is continuously increasing. According to the International Energy Agency (IEA), this global demand will increase by more than one-fourth by 2040 [1]. In order to meet the increasing demand while limiting the greenhouse gas emissions, a proper energy mix is required, and this incorporates geothermal, tidal, solar and wind energy along with other conventional energy sources. However, wind energy is one of the most promising alternative energy sources. The wind is purely renewable and is maintained and dominated by solar energy mainly through the uneven solar radiation across the Earth that forms the temperature gradient between the equator and the poles. This forms a pressure gradient where the cold and hot air streams are circulated due to buoyancy forces [2]. The wind turbines haven't the problem of either emitting the greenhouse gases, such as fossil fuel power plants, or having radiative waste, such as nuclear power plants. Therefore, increasing the wind energy share of the installed energy capacity assists in reducing climate change and environmental pollution and it is not limited to the daytime, such as solar energy. However, the wind energy potential depends on the location and changes with the seasons over the year. Hence, a proper energy mix is essential to cover the energy demand regardless of the uncertainty in the wind and solar energy potentials. In order to achieve the most benefits from the wind energy resources, there is a need to

develop and employ efficient wind turbine designs as a part of a sustainable energy mix in order to meet the growing energy demand. There is an increasing research interest in wind energy conversion and grid connections [3]–[7].

In contrast to Horizontal Axis Wind Turbines (HAWTs), small Vertical Axis Wind Turbines (VAWTs) have some important features, especially for the use in the urban environment, and this includes their better response to the high turbulence level and the rapid change in the urban flow conditions [8], [9]. In addition, the VAWT concept has a lower noise emission [8] and better integration with the building environment [10].

VAWTs can be classified to be the Savonius and Darrieus designs. The Darrieus VAWTs are based on the aerofoil-shaped blades that are driven by the lift forces and offers better performance in contrast to the drag driven Savonius designs. The straight blade Darrieus VAWTs features simple blade shape and easy construction and this type of VAWT is the focus of this paper.

Currently, VAWTs power coefficients lack behind that of the HAWTs, but increasing research has been established in order to enhance VAWTs performance. Computational Fluid Dynamics (CFD) has been frequently used for turbine flow analysis and optimization [11]–[16]. A range of other modelling approaches with different fidelity has also been used to predict the performance of VAWTs and this includes the Double Multiple Stream Tube (DMST) [17]–[19] and the vortex method [20], [21]. CFD has been found to be a powerful tool for the analysis, design, and optimization of the VAWT blades [22], [23] that enable more accurate predictions and detailed visualization [24]. Due to the simple geometry of the straight blade Darrieus VAWT, most of the current CFD modelling of VAWT is based on a 2D analysis [24]. However, most VAWT designs have a low aspect ratio. The 2D simulations ignore the important contributions of the blade tip effects and can result in significant errors.

2. Literature survey

Paillard et al. [25] studied the effect of three different viscous models in their CFD modelling of VAWT and this investigation includes the laminar model, SST k-ω turbulence model, and SST transition model. They found that the laminar model is associated with high oscillations and early stall predictions, and therefore it was concluded that the use of the laminar model was not suitable for their simulations. On the other hand, their simulations using the transition model showed some contradictory results, since the transition model results were associated with deeper stall and large recirculation zones. Moreover, they found that the transition model over-predicts the stall induced separation. They expected that either the inlet turbulence level needs to be adjusted or the transition model is not suitable for their cases. However, their results showed that the non-transition model, namely the SST k-ω, could give good agreement with the experimental data. In addition, Firdaus et al. [26] performed a 2D-CFD study of the VAWT that included the effect of different turbulence models, including RNG k-ε, Realizable k-ε, and SST k-ω. Their RNG k-ε results tended to have a better agreement with the experimental data in contrast with the

other investigated turbulence models. However, all the models appeared to significantly over-predict the turbine performance due to ignoring the three-dimensionality of the flow.

Howell et al. [27] compared both 2D and 3D CFD predictions of the power curve against the experimental data at low Reynolds number, as low as 30,000, based on the k–ε RNG turbulence model. The geometry of the straight blade Darrieus VAWT is symmetrical about its mid-span section and hence the use of symmetric boundary conditions enables the modelling of only one-half of the geometry in order to reduce the computational cost without sacrificing the accuracy for 3D simulations [27]. Their results showed that the 2D predictions of the power coefficient are significantly over-estimated while the 3D predictions had a good agreement with the experimental data in both trend and magnitude. However, the 3D predictions of the power coefficient showed some under-estimation in contrast with the experimental data at relatively high TSRs. Siddiqui et al. [28] quantified the differences in the predictions of the 2D and 3D CFD simulations with and without the consideration of the supporting structure based on the K-ε Realizable model. They found that the 2D results had an over-prediction by about 32% in the overall performance coefficient in contrast with the 3D simulations that resolved the supporting structure and tip losses. Franchina et al. [29] compared the 2D and 3D predictions of the velocity magnitude and turbulent intensity in the VAWT wake based on the SST K-ω with low Reynolds number correlations against the experimental data. They considered the use of a transitional turbulence model beyond the scope of their investigation. Their 2D results show a clear overestimation of the velocity in the wake region. While there are few comparative studies between the 2D and 3D predictions, almost each of these studies uses a specific turbulence model based on either its reputation or based on a recommendation from previous 2D studies. Hence, there is a lack of the assessment of how the quality of the turbulence models' predictions are different between the 2D and 3D cases.

Rezaeiha et al. [30] presented a critical 2D CFD comparison of seven commonly-used turbulence models mainly against the experimental data of the strength of the circulation of the vortex, time-averaged streamwise velocity in the wake region and the power coefficient over TSR. They concluded that the SST k-ω model and transitional variants are most suitable for URANS simulations. Almohammadi et al. [31] compared the 2D CFD predictions based on the SST k-ω and the SST transition turbulence model. They concluded that the transitional effect is essential for the prediction of the dynamic stall. However, their conclusion is based on the interpretation of the differences between the numerical results rather than a comparison with detailed experimental data. Daróczy et al. [32] carried out a 2D comparative CFD study based on six different turbulence models against four sets of experimental data. However, all these experimental data sets are limited to the power coefficient variations with the TSR. They found that the results of the k-ε Realizable model have consistence agreements with the four experimental data, while the results of the SST k-ω model did not match well with one of the four sets of experimental data. They suggested that further 3D assessments are needed before the final selection

of the suitable turbulence model. Several studies compare the suitability of the different turbulence model for vertical axis water turbines [33]–[35] and they obtained different conclusions about the most appropriate turbulence model for the vertical axis water turbine simulation. It is noticed that the majority of the turbulence model comparisons are based on the experimental data of the cycle-averaged power coefficient at different TSR. However, the cycle-averaged power coefficient is an integral quantity that may involve counteracting terms that affect the conclusion. Therefore, the use of more detailed experimental data will assist to have a better assessment of the quality of the turbulence models' predictions.

The aim of this study is to investigate the quality of the 2D and 3D CFD predictions of the SST K-ω model and the SST K-ω with the γ Intermittency transition against detailed experimental data. The selected experimental data are obtained by Li et al. [36] and this includes the pressure distribution around the turbine blade mid-span section based on a high-frequency multiport pressure scanner. In addition, the instantaneous single-blade torque coefficient is considered based on the pressure data at the mid-span section. The use of the data at the mid-span section enables a fair base of comparisons between the experimental data and the 2D CFD data due to the fact that the 3D effects are minimal at the mid-span section. In addition, this study aims to investigate how the behaviour of the SST K-ω with the γ intermittency transition model changes between the 2D and 3D cases.

3. 2D CFD Modelling

3.1. Model description and numerical methods

A two-bladed VAWT with a 6˚ fixed pitch is selected due to the availability of the detailed experimental data collected by on a high-speed multi-port pressure scanner. The turbine has a diameter of 1.7 m with NACA0015 aerofoil-profiled blades [36]. Figure 1 shows a 2D schematic of the rotor and the reference azimuthal locations. The cyclic motion of the turbine may be divided into two parts, particularly the upstream part between ϕ= 0° and ϕ= 180° and the downstream part between ϕ= 180° and ϕ= 360°. The selected reference test case corresponds to the optimum operating condition of the turbine with a wind speed of 7 m/s and a Tip Speed Ratio (TSR) of 2.29. The averaged Reynolds number based on the blade chord and the averaged theoretical relative velocity is about 2.5×105 and hence the flow is considered to be in the transition regime.

The baseline computational domain size is selected so that the domain boundaries are far enough away to eliminate any interference with the flow around the turbine. Figure 2 illustrates the size of the computational domain, the different subdomains and the adjacent boundary conditions. The domain size is extended downstream of the rotor to accommodate the turbine wake. The domain is divided into four subdomains, which represent the two blade-zones, the rotor zone, and the surrounding zone. These subdomains are connected via a set of non-conformal mesh interfaces. The Sliding Mesh method [37] is used to model the rotation of the turbine by imposing a constant rotation speed of about 18.9 rad/s to the rotor subdomain to match with the experimental

conditions and a velocity inlet boundary condition is associated to the upstream edge of the domain with a 10 m/s magnitude and 0.5% turbulence intensity. The downstream edge of the domain is defined as a pressure outlet boundary condition with zero gauge pressure. The lateral edges of the domain are defined as frictionless symmetric boundary conditions where zero gradients of the flow variables are imposed.

A fully structured mesh is used for the 2D model. The baseline mesh, with 920,600 total number of elements, has 1,000 nodes along each blade profile with a growth rate of 1.05 and a unity maximum dimensionless wall distance, y+, to ensure a well capturing of the boundary layer details around the blades. Figure 3 shows the mesh clustering near the blade while Figure 4 shows the baseline mesh distribution across the entire domain. The mesh is clustered near the rotor and in the wake region.
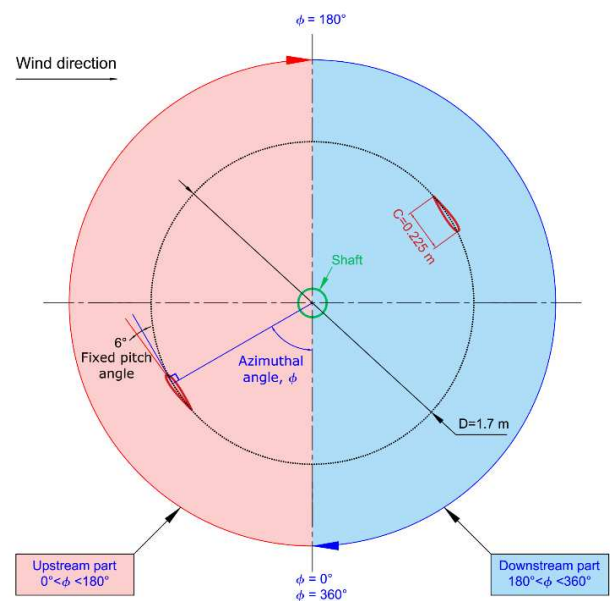

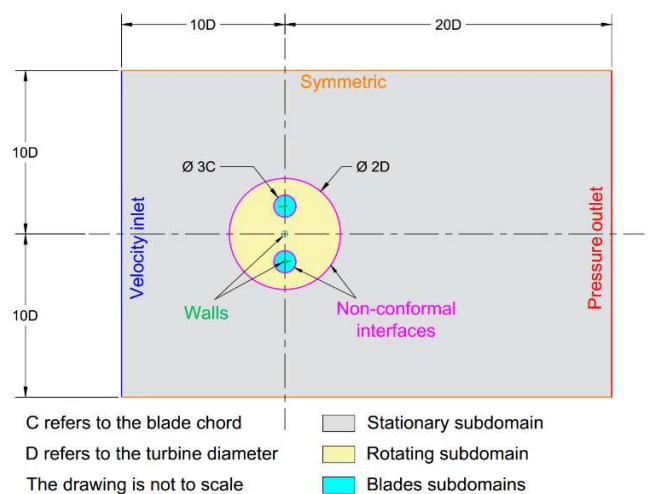**Figure 1** A 2D schematic of the selected turbine at an arbitrary azimuthal location.

Figure 2 A schematic of the 2D baseline computational domain and the associated boundary conditions.
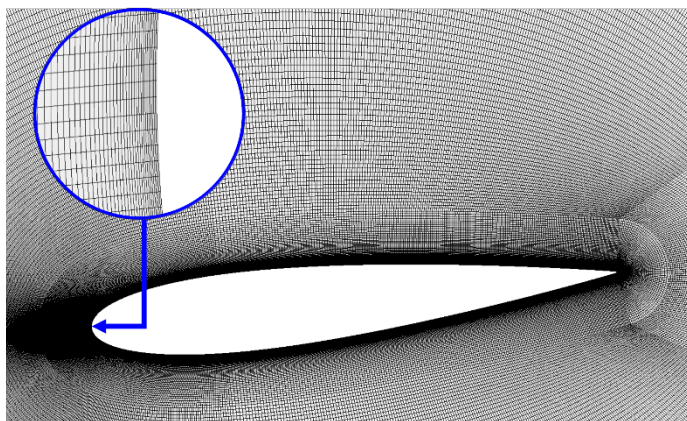
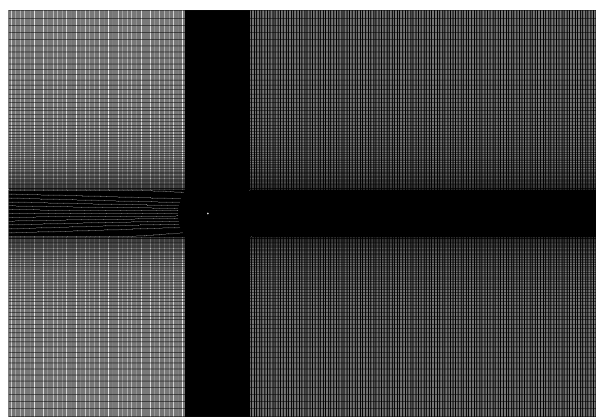**Figure 3** The baseline mesh near a blade with a pitch angle of 6º.

Figure 4 The mesh baseline of the whole domain showing the mesh clustering around the rotor and in the wake region.

Table 1 The CFD model specifications.

	Model specifications	Notes
Solver	Double-Precision Pressure-Based Solver	The Pressure-Based Solver accounts for the incompressible flow around the VAWT.
Pressure-Velocity coupling	Coupled	This enables the use of higher time-step size [37] and hence reduces the computational cost.
Moving Zone Modelling	Sliding Mesh	This is more robust in contrast with Overset and Dynamic Meshing.
Spatial discretization	2nd order upwind	This is justified in Section 0.
Temporal discretization	2nd order Implicit	The implicit formulation is unconditionally stable regardless of the time-step size [38]
Temporal resolution	540 time-step/cycle	This is justified in Section 0.
No. of iterations	30 iterations/time-step	This is found sufficient to reduce the residual of the main flow variables below 1e-5.

The simulations are performed using ANSYS FLUENT. Table 1 shows the specification of the CFD model. Two turbulence models have been investigated including the widely used SST k-ω turbulence model and the three equations SST k-ω with the γ transition turbulence model in order to account for the laminar to turbulent transition. In contrast with the four equation SST transition turbulence model, the SST k-ω with the γ transition turbulence model is recommended where moving walls exist within the domain [37]. In the present study, it is found that the results based on the two selected models have different behaviour and hence the two selected models are included in the verification of the different aspects of the computational model.

3.2. Solution periodicity

The flow-field is initialized using the Hybrid Initialization [37] relative to the absolute reference frame, which provides a good initial estimate of the velocity field based on the Laplace Equation [37]. While the VAWT encounters a periodic motion, some unsteadiness is expected in the first few cycles of the simulation as it starts with relatively simple initial conditions. Figure 5 shows the single blade torque ripple over the first ten cycles for the two selected turbulence models. For the upstream parts of the cycles, it is observed that the differences in the torque coefficients between the successive cycles are minimal after the first three cycles. However, notable differences are found in the downstream parts of the cycles. These differences in the downstream part of the cycles are partially associated to the interaction with the shaft wake and are further investigated in this paper.

Figure 6 (a) shows a comparison between the torque coefficient over the 5th and 6th cycles based on the SST k-ω model. Notable differences are found near $\phi= 270°$ where the blade passes through the shaft wake. Figure 6 (b) shows the counters of the vorticity magnitude at $\phi= 270°$ and this visualizes the wake interaction between the wake released from the turbine shaft and the downstream blade. In order for the assessment of the shaft effect on the solution periodicity in the downstream parts of the cycles, another set of mesh is constructed with the same meshing attributes without the shaft geometry.
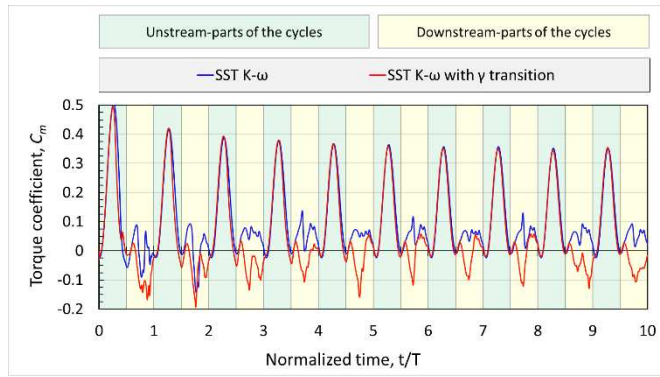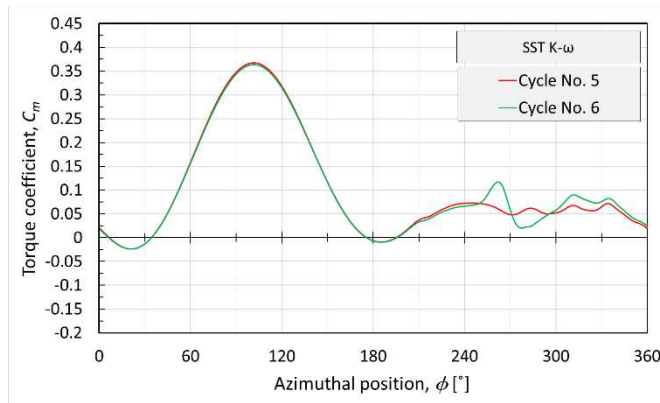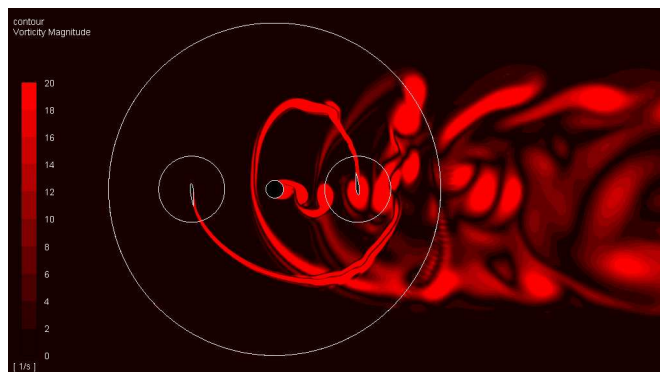
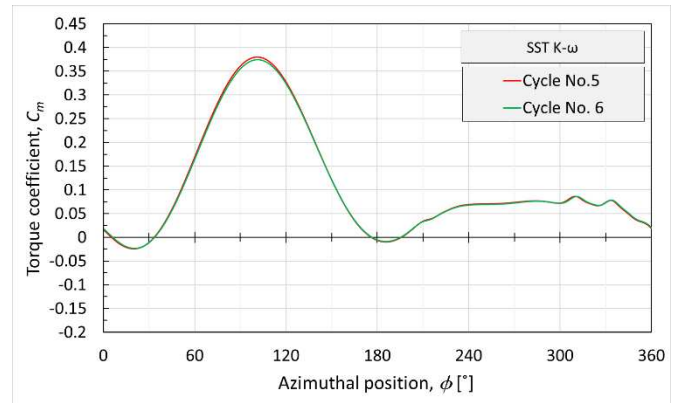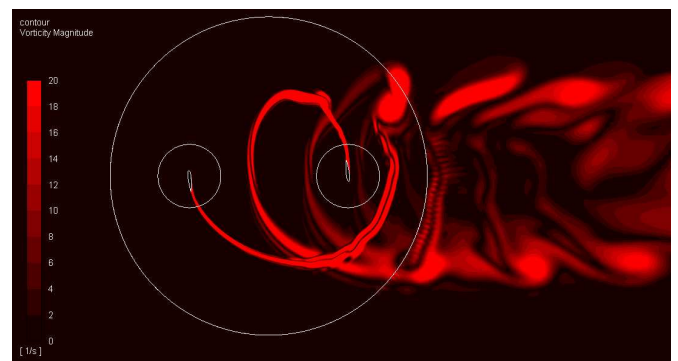**Figure 5** The single blade torque coefficient for the first 10 cycles.

(a)

(b)

Figure 6 (a) The single blade torque coefficient, Cm at the 5th and 6th cycles (b) Vorticity magnitude contours in the 5th cycle at 270º azimuthal position.

Figure 7 (a) shows a comparison between the torque coefficient over the 5th and 6th cycles based on the SST k-ω model. It is observed that the differences between the torque coefficient in the two cycles are minimal even in the downstream part of the cycles. It is observed that the differences between the successive cycles in Figure 6 (a) is because the wake released from the blades is not synchronized with that released from the shaft. Therefore, the upstream parts of the cycles are considered for the model verifications. In order to quantify how a certain model setting affects the average torque coefficient in the upstream part of the cycle, a sensitivity parameter is introduced as follow:

$$Sensitivity = \frac{c_m|_{new\,setting} - c_m|_{baseline\,setting}}{c_m|_{baseline\,setting}}\Bigg|_{at\,the\,upstream\,part} \times 100\% \qquad (1)$$

(a)

(b)

Figure 7 (a) The single blade torque coefficient, C_m at the 5th and 6th cycles without the modelling of the shaft. (b) Vorticity magnitude contours in the 5th cycle at 270º azimuthal position.

The baseline setting is considered suitable if the sensitivity drops below 1% in the 2D case or 2% in the 3D case in contrast with any higher fidelity or higher-order setting. In order to select the minimum number of cycles required for a time-periodic solution, the sensitivity of the average torque coefficient in the upstream part to the number of cycles is quantified. The solution is considered time-periodic at the 5th cycle based on the SST k-ω turbulence model and the 6th cycle based on the SST k-ω with the γ transition turbulence model where the sensitivities between the successive cycles drop below 1%. Hence, these selected cycles are used for the post-processing in the further tests. It appears that the use of the Coupled Scheme in addition to the Hybrid Initialization assists in reducing the required number of cycles for the time-periodic solution in contrast with the 20 to 30 cycles requirement in some other research that use the Semi-Implicit Method for Pressure Linked Equations (SIMPLE) Scheme [39].

3.3. Effect of domain size

In order to investigate the effect of the domain size on the predicted results. Two parameters, ℓa and ℓb, are used to parametrize the domain size as shown in Figure 8. Three different domain sizes are selected, namely Small, Baseline, and Extended Domains. The details of these different domains and the sensitivities of the torque coefficient to the domain

size are summarized in Table 2. It is found that the sensitivity of the results to the change from the baseline domain to the extended domain is about 1% based on the two turbulence models. Hence, the baseline domain is considered to be large enough to minimize the influence on the results and is selected for the further tests. Figures 9 (a) and (b) shows the influence of the domain size on the instantaneous torque coefficient based on the two selected turbulence models. It appears that the results based on the SST k-ω with the γ transition turbulence model are more sensitive to the change in the domain size, especially in the downstream part of the cycle.

Table 2 The details of the selected domains and the torque coefficient sensitivity based on the upstream part of the cycle where D is the turbine diameter.

	ℓ_a	ℓ_b	Sensitivity of the $\overline{C_m}$ in the upstream part of the cycle	
			SST k-ω	SST k-ω with γ transition
Small Domain	5D	10D	3.33%	3.27%
Baseline Domain	10D	20D	---	---
Extended Domain	20D	40D	-0.79%	1.02%

3.2. Verifications

The verification of a numerical model aims to assess the sources of numerical errors and how the different aspects of numerical modelling affect the predicted results. The results of a good time-dependent numerical model should achieve independence of the time-step size, mesh size, in addition to the order of the spatial and temporal discretization. The following subsections include several sensitivity tests in order to assess the solution independency.

3.2.1. Time step independency

In order to assess the time step independency of the 2D solution, four different temporal resolutions have been tested. These include 360, 540 (the baseline resolution), 720, and 1080 time steps per cycle, which correspond to 1, 1.5, 2, and 3 time steps per each degree of azimuthal angles, respectively. Table 3 shows the tested temporal resolutions and the corresponding physical time-step sizes. In contrast with the baseline case, Table 3 shows the sensitivity of the torque coefficient based on the upstream part of the cycle. It is observed that the sensitivities of the averaged upstream torque coefficient to the increase in the temporal resolution are less than 1% using the two turbulence models. Hence, the baseline temporal resolution is considered suitable for the further analysis.

Figures 10 (a) and (b) show the instantaneous torque coefficient for the different temporal resolution based on the two selected turbulence models. It is clear that the results based on the SST k-ω with the γ transition turbulence model

are more sensitive to the change in the temporal resolution. Despite the notable differences between the instantaneous torque coefficient curves in Figure 10 (b), these differences appear to diminish each other in the upstream part of the cycle where the differences in the average values are less than 1%. This behaviour of the diminishing differences is found also when the effect of the mesh size and the order of discretization are tested in the Subsections 0 and 0.
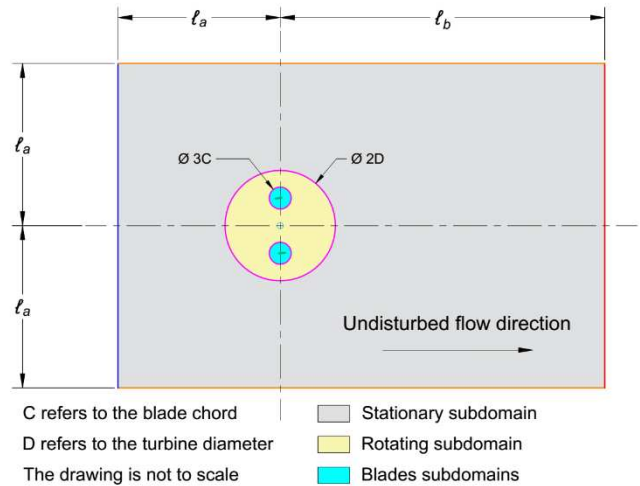

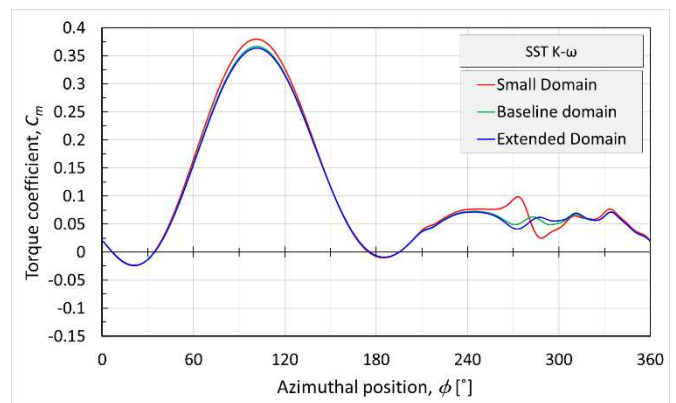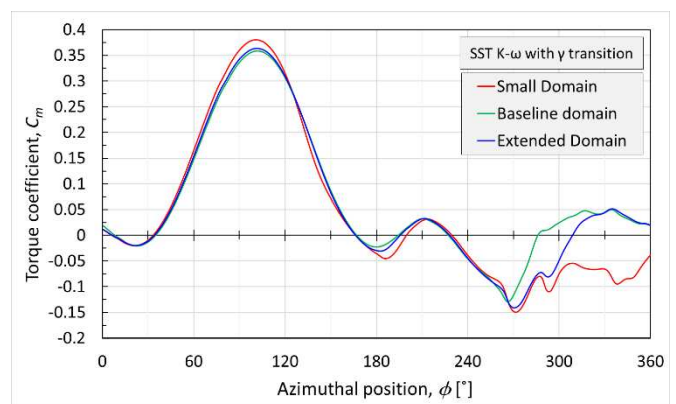**Figure 8** The 2D computational domain showing the selected parameters ℓ_a and ℓ_b.
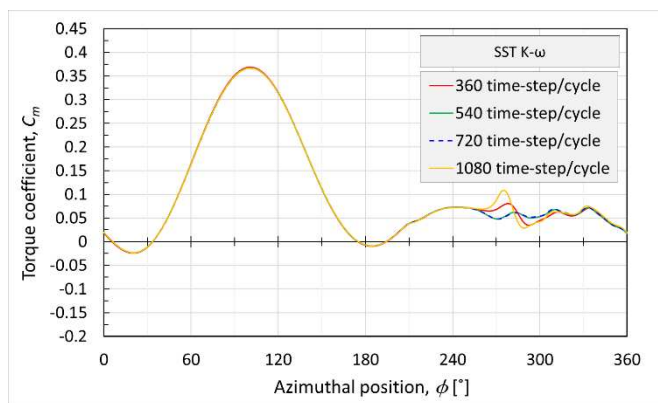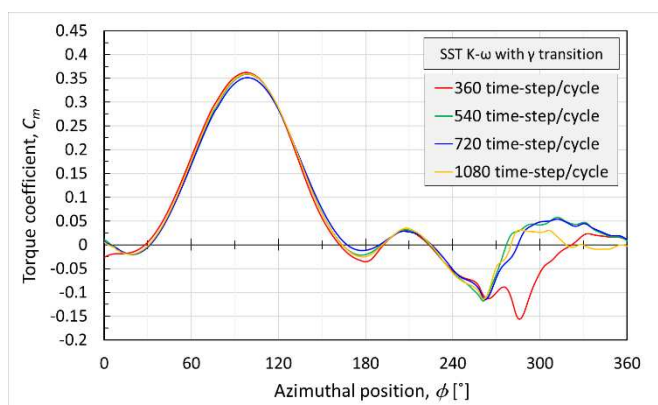

(a)

(b)

Figure 9 The influence of the domain size on the torque coefficient, C_m for (a) the SST k-ω and (b) the SST k-ω with the γ transition turbulence models.

Table 3 The tested temporal resolutions and the corresponding physical time-step sizes, in addition to the torque coefficient sensitivity based on the upstream part of the cycle.

No. of time steps per cycles [time step/cycle]	The physical time-step size [s]	No. of time steps per each degree of azimuthal angles [time step/°]	Sensitivity of the $\overline{C_m}$ in the upstream part of the cycle	
			SST k-ω	SST k-ω with γ transition
360	9.26×10^{-4}	1	0.44%	0.26%
540 (baseline)	6.17×10^{-4}	1.5	---	---
720	4.63×10^{-4}	2	-0.12%	-0.24%
1080	3.09×10^{-4}	3	+0.16%	%0.49

(a)

(b)

Figure 10 The influence of the temporal resolution on the torque coefficient, C_m for (a) the SST k-ω and (b) the SST k-ω with the γ transition turbulence models.

3.2.2. 2D mesh independency study

In addition to testing the mesh independency of the 2D solution, this study identifies the significance of the different mesh attributes. The advancement in the desktop computing hardware in addition to the availability of High-Performance Computing (HPC) facilities makes it affordable to carry out the 2D VAWT simulations even with a relatively fine mesh and temporal resolution. However, the 3D simulations have a substantially higher computational cost and an in depth attention should be given to the selection of the mesh sizing. The sensitivity study of the different mesh attributes in the

2D case assists in suggesting a suitable 3D mesh in order to build a computationally affordable 3D model.

In this mesh study, four mesh attributes are investigated that include: (i) the number of nodes around the blade profile, (ii) the Growth Rate (GR) of the mesh perpendicular to the blade profile, (iii) the dimensionless wall distance, y+, perpendicular to the blade profile, and (iv) the global Refinement Factor (RF). The global RF is applied to the edge sizes across the domain except for the inflation layer around the blade in order to maintain the GR and y+. In addition to the baseline mesh, ten sets of mesh are constructed to test the effect of the selected mesh attributes. Table 4 shows the details of these sets of mesh in addition to the sensitivity of the upstream torque coefficient to the change in the relevant meshing attribute based on the two turbulence models.

In contrast with the baseline mesh, it is observed that the sensitivities of the averaged upstream torque coefficient to the chordwise refinement and the reduction of GR are less than 1.0 % based on the two turbulence models. However, the sensitivity of the averaged upstream torque coefficient to increasing the global RF from RF= 1.0 in the baseline to RF=2.0 in the fine mesh are about 1.07 and 0.19 for the SST k-ω and the SST k-ω with the γ transition turbulence models, respectively. The number of mesh elements of the tested fine mesh is about 3.1 times that of the baseline mesh and this substantially increases the computational cost. Although the sensitivity based on the SST k-ω model between the baseline mesh and the fine mesh slightly exceeds the desired limit of 1%, the baseline mesh is considered suitable for the further 2D analysis due to the trade-off between the accuracy and the computational cost.

It is observed from Table 4 that the averaged upstream torque coefficient is very sensitive to the changes of y+. It is observed that the results of the SST k-ω with the γ transition turbulence model is usually more sensitive to the change in the mesh attributes in contrast with the SST k-ω turbulence model. Figures 11 (a) and (b) show the effect of the global mesh refinement on the instantaneous torque coefficient based on the SST k-ω model and the SST k-ω with the γ transition turbulence model, respectively. In contrast with the results of the SST k-ω model, it is clear that the results of the SST k-ω with the γ transition turbulence model are generally more sensitive to the mesh refinement, especially on the downstream part of the cycle where strong wake interactions exist.

Table 4 The specifications of the tested 2D meshes in addition to the sensitivity of the predicted results.

Name	Features and the total number of elements	No. of nodes around the aerofoil	Maximum y+ at the maximum theoretical relative velocity point	Sensitivity of the $\overline{C_m}$ in the upstream part of the cycle	
				SST k-ω	SST k-ω with γ transition
Mesh 2D-A1	Baseline mesh (920600 elements)	1000	≈ 1	---	---
Mesh 2D-A2	Refined chordwise (1105600 elements)	1500	≈ 1	-0.18	-0.67
Mesh 2D-A3	Coarsened chordwise (735600 elements)	500	≈ 1	0.62	1.9
Mesh 2D-A4	Coarsened chordwise (624600 elements)	200	≈ 1	0.66	8.28
Mesh 2D-A5	Lower growth rate (GR=1.03) (1030600 elements)	1000	≈ 1	-0.21	-0.995
Mesh 2D-A6	Higher growth rate (GR=1.1) (828600 elements)	1000	≈ 1	0.41	4.04
Mesh 2D-A7	Higher growth rate (GR=1.2) (774600 elements)	1000	≈ 1	0.55	2.66
Mesh 2D-A8	Higher y+ (764600 elements)	1000	≈ 25	-6.19	-2.18
Mesh 2D-A9	Extra higher y+ (732600 elements)	1000	≈ 60	-22.97	-11.28
Mesh 2D-A10	Coarse mesh (RF=0.5) (292300 elements)	500	≈ 1	-0.13	2.97
Mesh 2D-A11	Fine mesh (RF=2.0) (2854400 elements)	2000	≈ 1	1.07	0.19

3.2.3. Effect of the order of the spatial and temporal discretization

In order to verify the accuracy of the current 2D CFD model, the predicted results are compared against the results obtained by lower and/or higher-order discretization schemes. As mentioned in Table 1, the current CFD model utilizes the second-order upwind scheme for the spatial discretization as well as the second-order implicit scheme for the temporal discretization. Figures 12 (a) and (b) show the instantaneous torque coefficient based on the SST k-ω model and the SST k-ω with the γ transition turbulence model, respectively, using the First Order Upwind, Second-Order Upwind and the Third-Order Quadratic Upstream Interpolation for the Convective Kinematics (QUICK) spatial discretization schemes. Again, the results of the transition model are more sensitive. However, the results of the second and third order schemes are relatively very similar for the two models. Hence, the second-order spatial discretization is considered adequate for the further analysis.

Regarding the temporal discretization, the instantaneous torque coefficient predictions using the First and Second-Order Implicit schemes are compared in Figures 13 (a) and (b) based on the SST k-ω model and the SST k-ω with the γ transition turbulence model, respectively. The comparisons show that the order of the temporal discretization has notable effects, especially in the downstream part of the cycle, and these effects are much higher in the case of the transition model. Therefore, Second-Order Implicit schemes are selected for the further analysis.

4. 3D CFD modelling

4.1. Model description

The 3D CFD model has the same numerical specification of the 2D model that is clarified in Section 3.1. For straight-bladed VAWTs, the mid-span plane splits the rotor geometry into two symmetrical halves. In the current 3D model, only the upper half of the rotor is modelled in order to reduce the computational cost. This is achieved by applying the

symmetric boundary condition to the mid-span plane. The locations of the main boundary conditions and dimensions of the 3D domain are illustrated in Figure 14. The dimensions of the mid-span plane of the 3D domain are adopted from the baseline 2D domain, which have been verified to be large enough to have a negligible effect on the predicated results in Section 0. In addition, the height of the 3D domain is chosen to be as large as 10 turbine diameters and this is equivalent to 17 turbine heights. The 3D domain is divided into four subdomains and these include the surrounding and rotor subdomains in addition to a subdomain around each of the two blades. These subdomains facilitate the modelling of the turbine rotation and blade pitch if required.

4.2. 3D mesh and mesh independency study

Structured mesh topologies are mainly used for the rotor and blades subdomain. Figure 15 (a) and (b) show the mesh clustering around the blade and the adjacent arm in the 3D baseline mesh in addition to the mesh clustering near the blade tip. In contrast with the unstructured mesh, the structured mesh enables one to have more control in the sizes and distributions of mesh elements and this assists in implementing very fine boundary mesh distributions perpendicular to the blade surface where the gradients of the flow field variables are high.
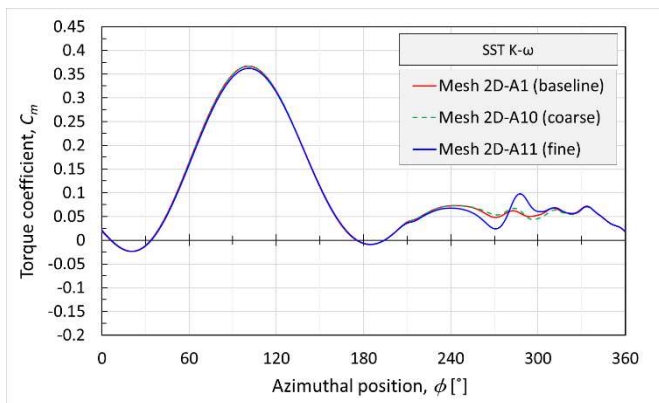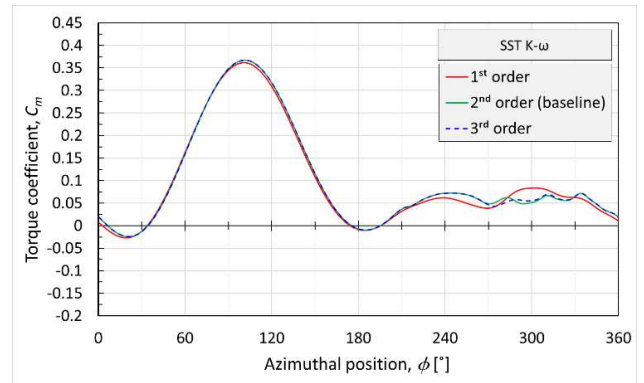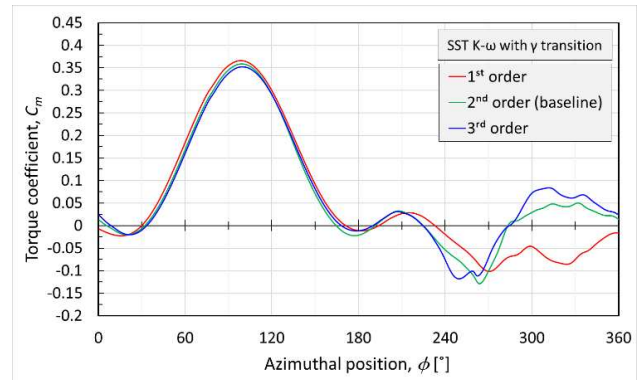

(a)
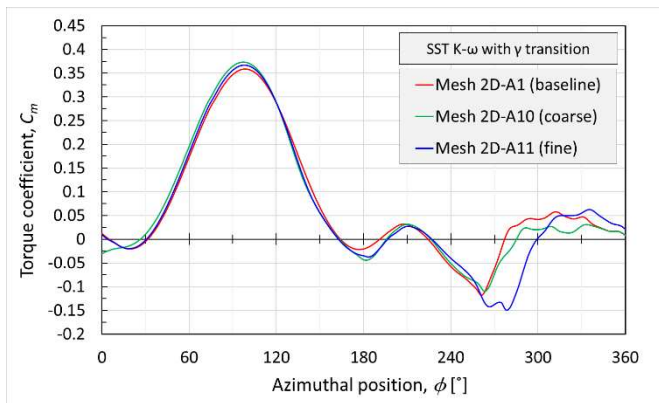
(b)

Figure 11 The influence of the 2D mesh refinement on the torque coefficient, C_m for (a) the SST k-ω and (b) the SST k-ω with the γ transition turbulence models.

(a)

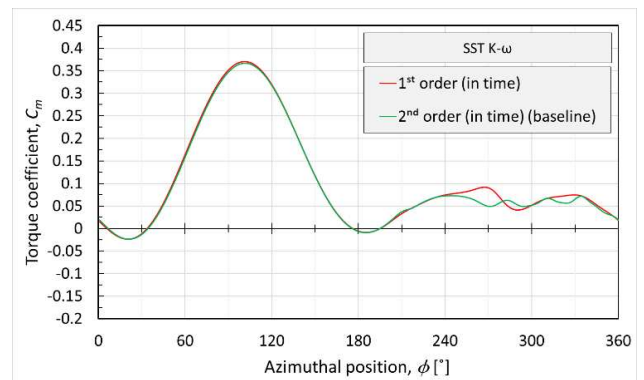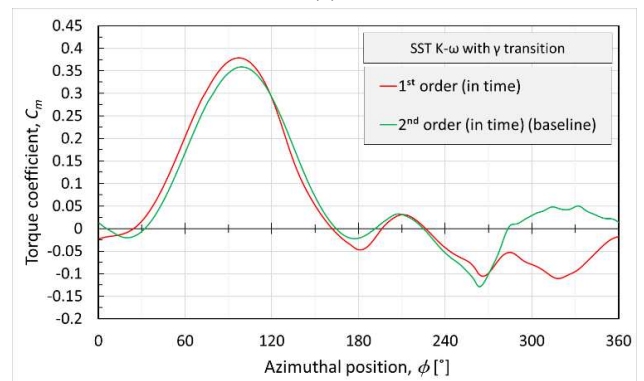
(b)

Figure 12 The influence of the order of spatial discretization on the torque coefficient, C_m for (a) the SST k-ω and (b) the SST k-ω with the γ transition turbulence models.

(a)

(b)

Figure 13 The influence of the order of temporal discretization on the torque coefficient, C_m for (a) the SST k-ω and (b) the SST k-ω with the γ transition turbulence models.
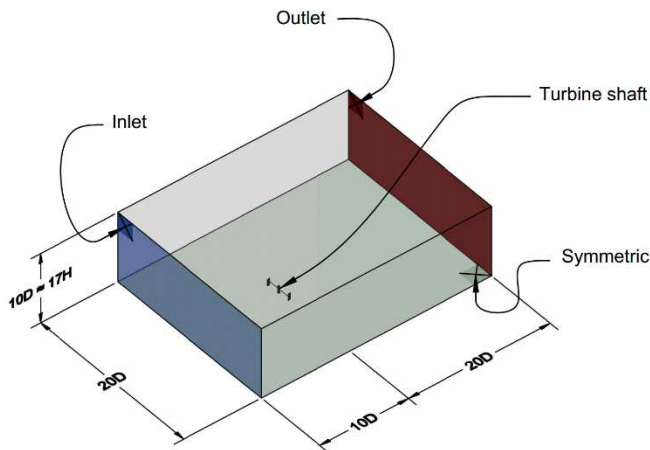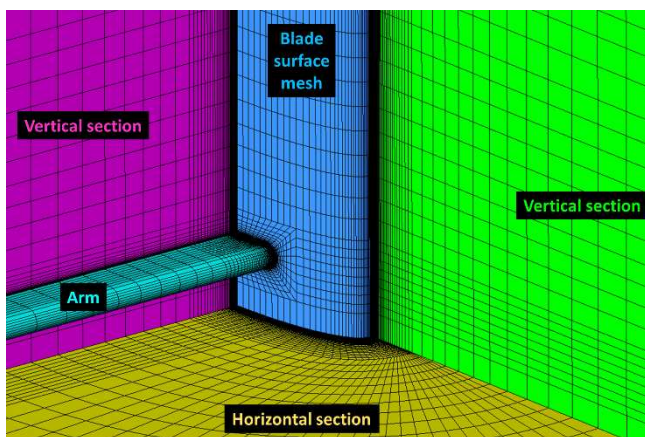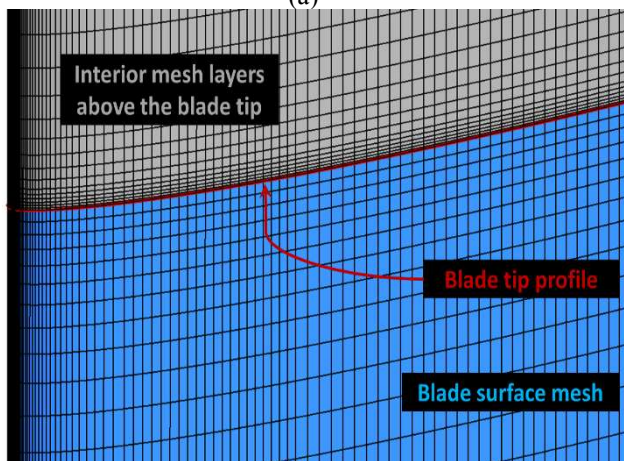
Figure 14 The 3D computational domain and the associated boundary conditions (not to scale).

(a)

(b)

Figure 15 The 3D baseline mesh (a) around the blade and adjacent arm and (b) near the blade tip.

In addition, the use of structured mesh enables the use of coarse mesh distributions in the spanwise direction in which the changes in the flow field variables are relatively low. However, the mesh is clustered in the spanwise direction near the blade tip in order to accurately capture the tip flow. Therefore, the use of structured mesh topologies enables the construction of a computationally efficient mesh that minimizes the total number of elements while maintaining adequate mesh resolution in the regions with high gradients.

On the other hand, the surrounding subdomain size is substantially larger. Hence, the CutCell meshing [40] is used in the surrounding subdomain and this enables the use of high growth rates while maintaining a good mesh quality. Figure 16 shows the CutCell mesh and the different cell sizes on the symmetric plane in the surrounding subdomain. This illustrates how the CutCell meshing is an efficient technique to make the transition from a relatively fine mesh near the rotor and the wake region to a coarse mesh elsewhere without compromising the mesh quality.

Based on the analysis of the sensitivity of the 2D results to the different mesh attributes and the trade-off between the accuracy and computational cost, the baseline 3D mesh is selected to have a GR of 1.1 and y+ <1 around the blades. The blade cross-sectional profile has 180 nodes and each blade half-height has 35 spanwise division that is clustered near the blade tip. The baseline 3D mesh has about 3.8 million mesh elements.

In order to test the mesh independency of the predicted results, two sets of mesh are constructed, namely the coarse and fine 3D meshes, which have RFs of 0.8 and 1.3, respectively. Table 5 shows the details of the tested 3D meshes in addition to the sensitivity of the upstream averaged torque coefficient to the change in the mesh RF. In contrast with the baseline 3D mesh, it is observed that the sensitivities of the averaged upstream torque coefficient to the global mesh refinement is less than 1.0 % in magnitude based on the two turbulence models. Hence, the baseline 3D mesh is considered adequate for the further 3D analysis. Figures 17 (a) and (b) show the effect of the 3D mesh refinement on the instantaneous torque coefficient based on the SST k-ω model and the SST k-ω with the γ transition turbulence model, respectively. Based on the SST k-ω with the γ transition turbulence model, it is observed that that the 3D model is less sensitive to the mesh refinement in contrast with the 2D model. This is clear in the comparison between the effects of the global mesh refinement in the 2D case in Figure 11 (b) against the 3D case in Figure 17 (b).
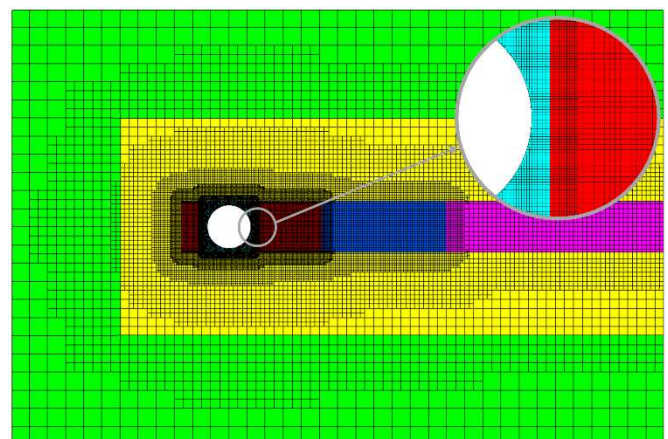

Figure 16 The baseline 3D mesh of the surrounding subdomain at the symmetric plane with a magnified view of the region near the rotor interface. The different colours represent different cell sizes, namely ▢ 0.2C, ▢ 0.4C, ▢ 0.8C, ▢ 1.6C, ▢ 5C, and ▢ 20C where C is the blade chord.

Table 5 The specifications of the tested 3D meshes in addition to the sensitivity of the predicted results.

| Name	Features and the total number of elements	Refinement factor	The ratio between the number of elements relative to the baseline mesh	Sensitivity of the $\overline{C_m}$ in the upstream part of the cycle	
				SST k-ω	SST k-ω with γ transition
Mesh 3D-A1	Baseline mesh (3,838,303 elements)	1	1	---	---
Mesh 3D-A2	Coarse mesh (2,540,426 elements)	$\sqrt[3]{0.5} \approx 0.8$	0.66	-0.2 %	-1.8 %
Mesh 3D-A3	Fine mesh (7,872,013 elements)	$\sqrt[3]{2.0} \approx 1.3$	2.05	-0.9 %	-0.6 %

(a)

(b)
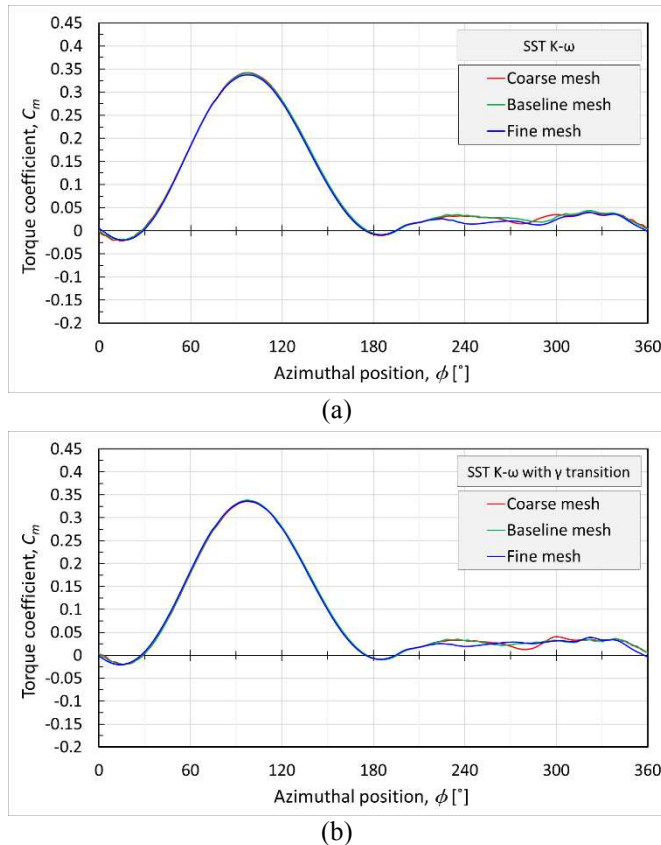
Figure 17 The influence of the 3D mesh refinement on the torque coefficient, Cm for (a) the SST k-ω and (b) the SST k-ω with the γ transition turbulence models.

5. Results and Discussions

In this section, the 2D and 3D CFD results using the two turbulence models are validated and discussed. The validation of the numerical model focuses on conceptual modelling errors and aims to assess the ability of the numerical model to represent the physical problem. Both the 2D and 3D models are validated against the experimental data obtained by Li et al. [36]. These experimental data are based on a high-speed multi-port pressure scanner. The data includes the pressure distributions around the blade at different azimuthal locations at the mid-span section, in addition to the pressure contribution to the instantaneous torque coefficient at several spanwise locations. In order to have a fair reference for comparisons, all the CFD predictions of the torque coefficient

in this section are based on the pressure contributions while the shear contributions to the torque coefficient are excluded.

At the mid-span section of the turbine blade, the 3D effects are minimal and hence the data at the mid-span section is most suitable for the comparisons with the 2D CFD predictions. The comparison between the experimental data and the CFD predictions using the two turbulence models are shown in Figures 18 (a) and (b) for the 2D and 3D cases, respectively.
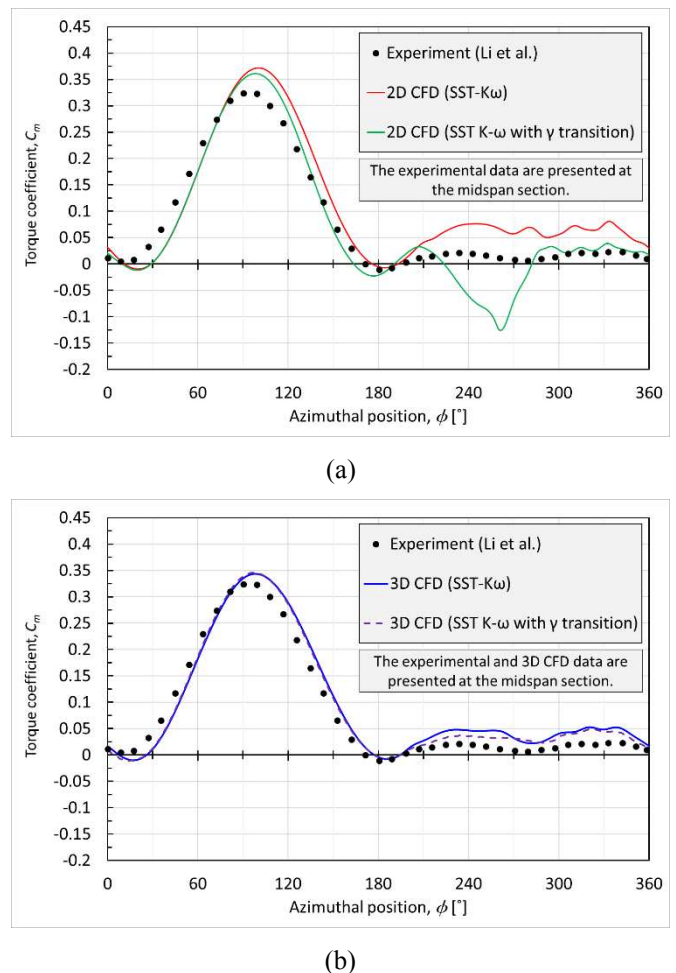

(a)

(b)

Figure 18 A comparison of (a) the 2D and (b) the 3D CFD results against the experimental data of torque coefficient at the blade mid-span section.

Under the current setup, it is observed that the 3D CFD predictions have an improved agreement with the experimental data in contrast with the 2D CFD predictions. In the upstream part of the cycle, the 2D CFD predictions based on the SST k-ω with the γ transition turbulence model are closer to the experimental data in contrast with the SST k-ω model case. However, the 2D CFD predictions based on the SST k-ω with the γ transition turbulence model have a strange trend in the downstream part of the cycle. For the 3D case, it is observed that the differences between the predictions based on the two turbulence models are minimal in the upstream part of the cycle.

In order to gain more insight on the differences between the 2D and 3D CFD predictions of the two turbulence models, the CFD predictions of the pressure coefficient around the blade mid-span are compared to the experimental data at different azimuthal positions with 30˚ interval as shown in Figures 19 and 20 for the upstream and downstream parts of the cycle, respectively. It is observed that the 2D CFD predictions have higher suction peaks near the leading edge of the blade. In contrast with the 2D and 3D CFD predictions based on the SST k-ω with the γ transition turbulence model, the suction peaks are generally higher in the cases of the SST k-ω turbulence model as observed in Figures 19 (a) and 20 (b-f). In contrast with the 2D CFD predictions, it is observed that the 3D predictions have a better agreement with the experimental data. In addition, the trends of the 2D predictions based on the SST k-ω turbulence model are similar to that of the experimental data. However, the trend of the pressure coefficient on the suction side based on the SST k-ω with the γ transition turbulence model deviates from the experimental data at ϕ= 150˚ where the blade passes through its own wake. In addition, the 2D predictions based on the SST k-ω with the γ transition turbulence model have strange trends in some locations in the downstream part of the cycle between ϕ= 210˚ and ϕ= 270˚ as shown in Figures 20 (b-d). This is related to the corresponding deviations in the torque coefficient in Figure 18 (a).
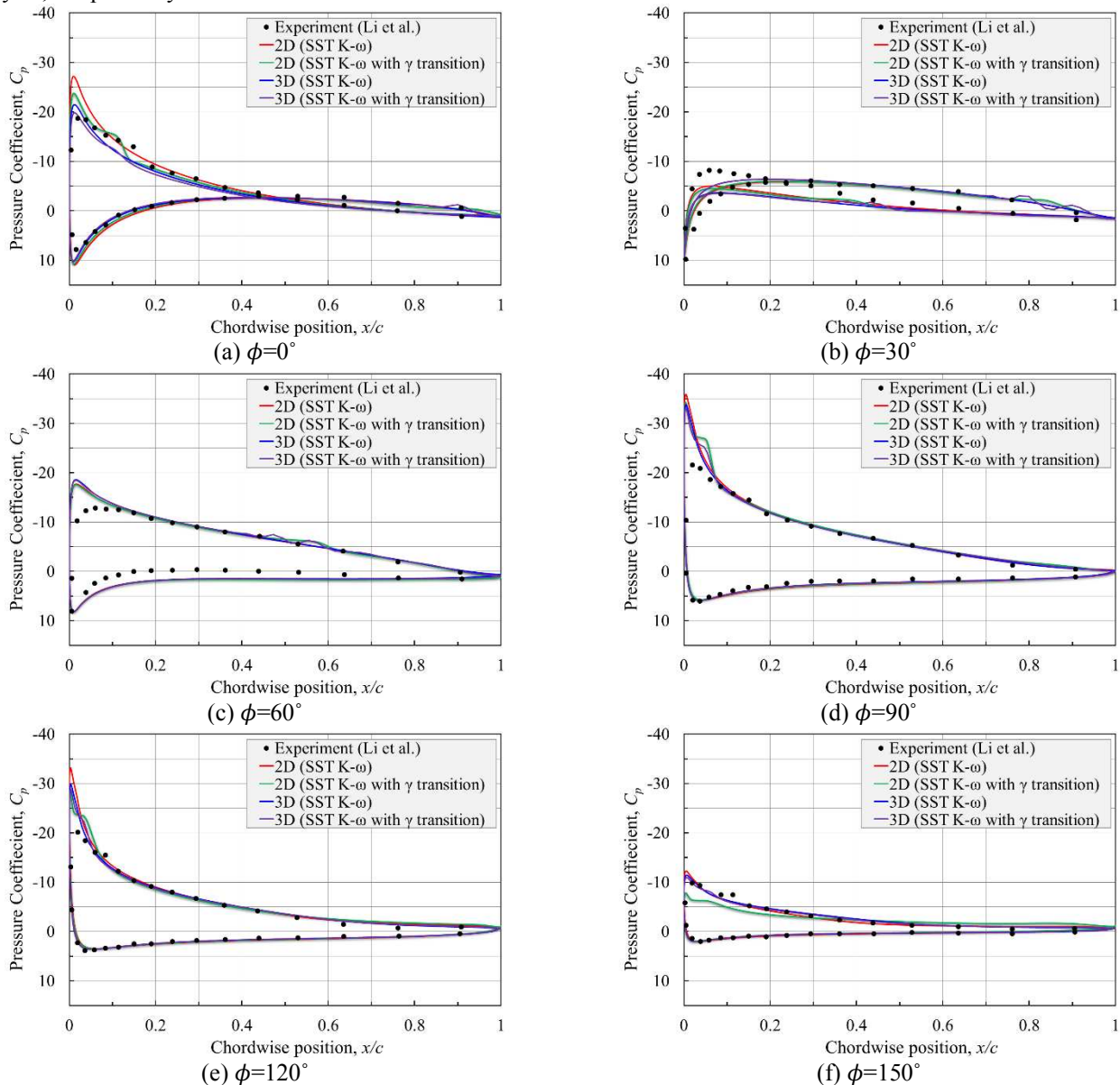

Figure 19 A comparison between the experimental, 2D and 3D CFD pressure coefficient around the blade mid-span section on the upstream part of the cycle.
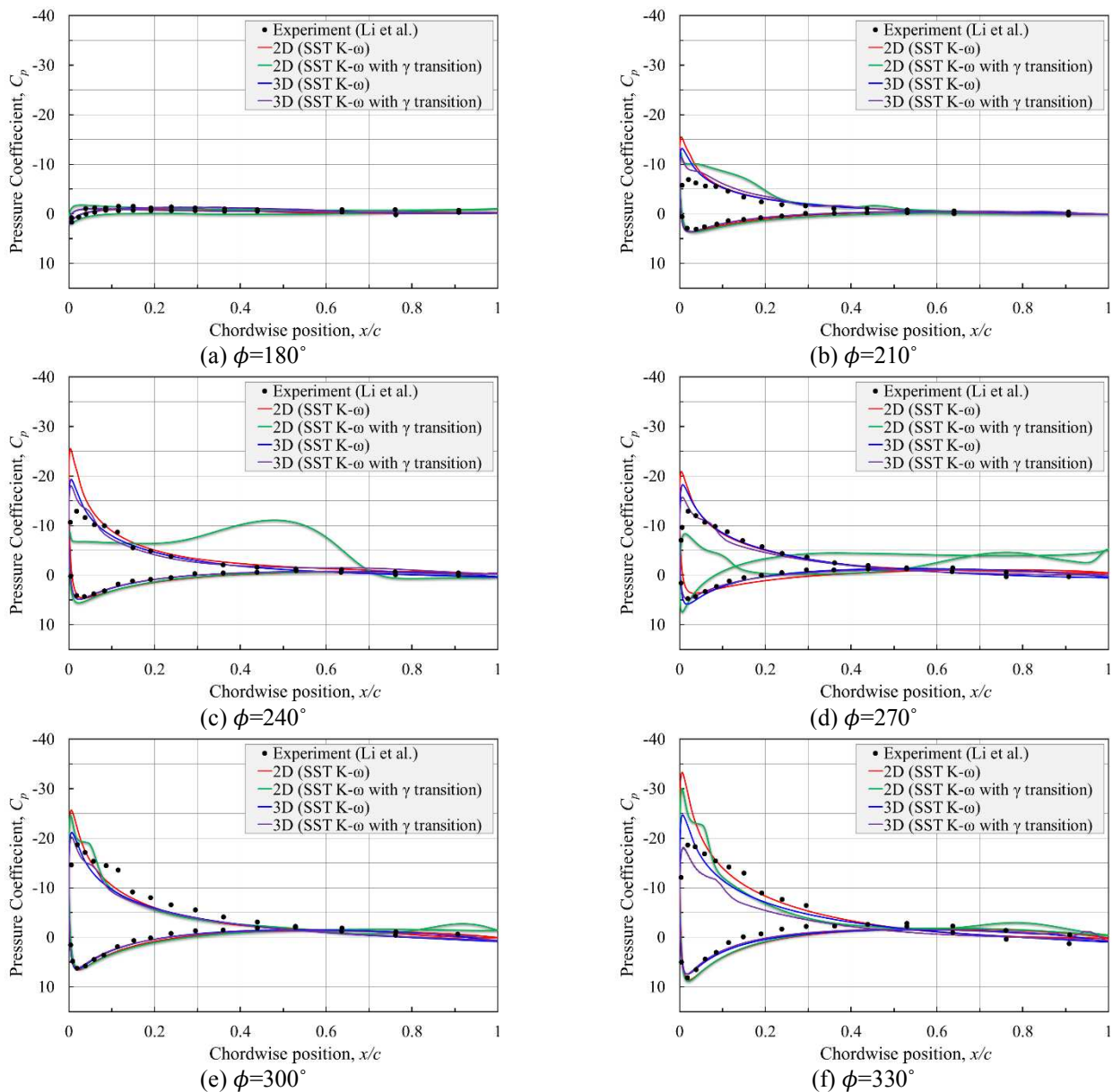
Figure 20 A comparison between the experimental, 2D and 3D CFD pressure coefficient around the blade mid-span section on the downstream part of the cycle.

It is observed that the 2D and 3D results based on the SST k-ω with the γ transition turbulence model are able to predict the existence of the Laminar Separation Bubbles (LSBs) that are found also in the experimental data as shown in Figures 19 (a, d-f) and 20 (e, f). However, the predicted locations of the LSBs are shifted towards the leading edge of the blade.

In order to facilitate the visual comparisons between the 2D and 3D results, CFD-Post software [41] is used to represent the 2D results in a 3D form where the flow variables are kept constant in the spanwise direction. While the 3D model only simulates the upper half of the rotor, CFD-Post software is used to mirror the data and to visualize the whole blade. Figures 21 (a, b, d, e) shows a visual comparison between the 3D and 2D flow pattern on the suction side of the blade for the two turbulence models at φ= 150°. The arrowheads illustrate the flow direction based on the relative velocity vector at a distance of 0.001 m above the suction side. The green lines visualize the boundaries of the reverse flow

zones, which directly indicate the existence of separation. The yellow areas represent the location of the arms. The red and blue relative velocity streamlines illustrate the flow near the blade tip. The differences between the 3D flow pattern based on the two turbulence models are minimal as observed in 21 (a, d). However, it is observed that there are considerable differences between the predicted 2D flow pattern based on the two turbulence models as shown in Figures 21 (b, e). The 3D representation of the 2D results based on the SST k-ω with the γ transition turbulence model shows an extended separation in contrast with that of the SST k-ω turbulence model.

In addition to the pressure coefficient distributions, Figures 21 (c, f) show the sizes of reverse flow zones based on the two turbulence models in the 2D case and around the mid-span section in the 3D case. It is observed, in Figure 21 (f), that the results based on the SST k-ω with the γ transition turbulence model over-predict the size of the reverse flow

zone in the 2D case at ϕ= 150°, where the 2D predictions of the pressure coefficient deviate from the experimental data on the suction side of the blade. It is concluded that unphysical separation is predicted in the 2D case based on the SST k-ω with the γ transition turbulence model at ϕ= 150°.

Similarly, Figures 22 (a-f) show the flow pattern and visualize the reverse flow zones at ϕ= 240°. In the 3D case, the predicted flow pattern near the blade tip based on the two turbulence models are different as shown in the streamlines in Figures 22 (a, d). It is observed that the results based on the SST k-ω with the γ transition turbulence model have a more complex flow near the tip and the red streamlines show a part of the tip flow moving inwards in the spanwise direction. In

the 2D case, the arrowheads in Figures 22 (b, e) illustrate the large differences between the prediction of the reverse flow zone based on the two turbulence models. In addition, Figures 22 (c, f) show the differences in the size and shape of the reverse flow zones based on the two turbulence models in the 2D case and around the mid-span section in the 3D case. It is observed, in Figure 22 (f), that the results based on the SST k-ω with the γ transition turbulence model have a large reverse flow zone near the leading edge that indicates a large Leading Edge Vortex (LEV) in the 2D case at ϕ=150°, where the 2D predictions of the pressure coefficient have a large deviation on the suction side of the blade in contrast with the experimental data.
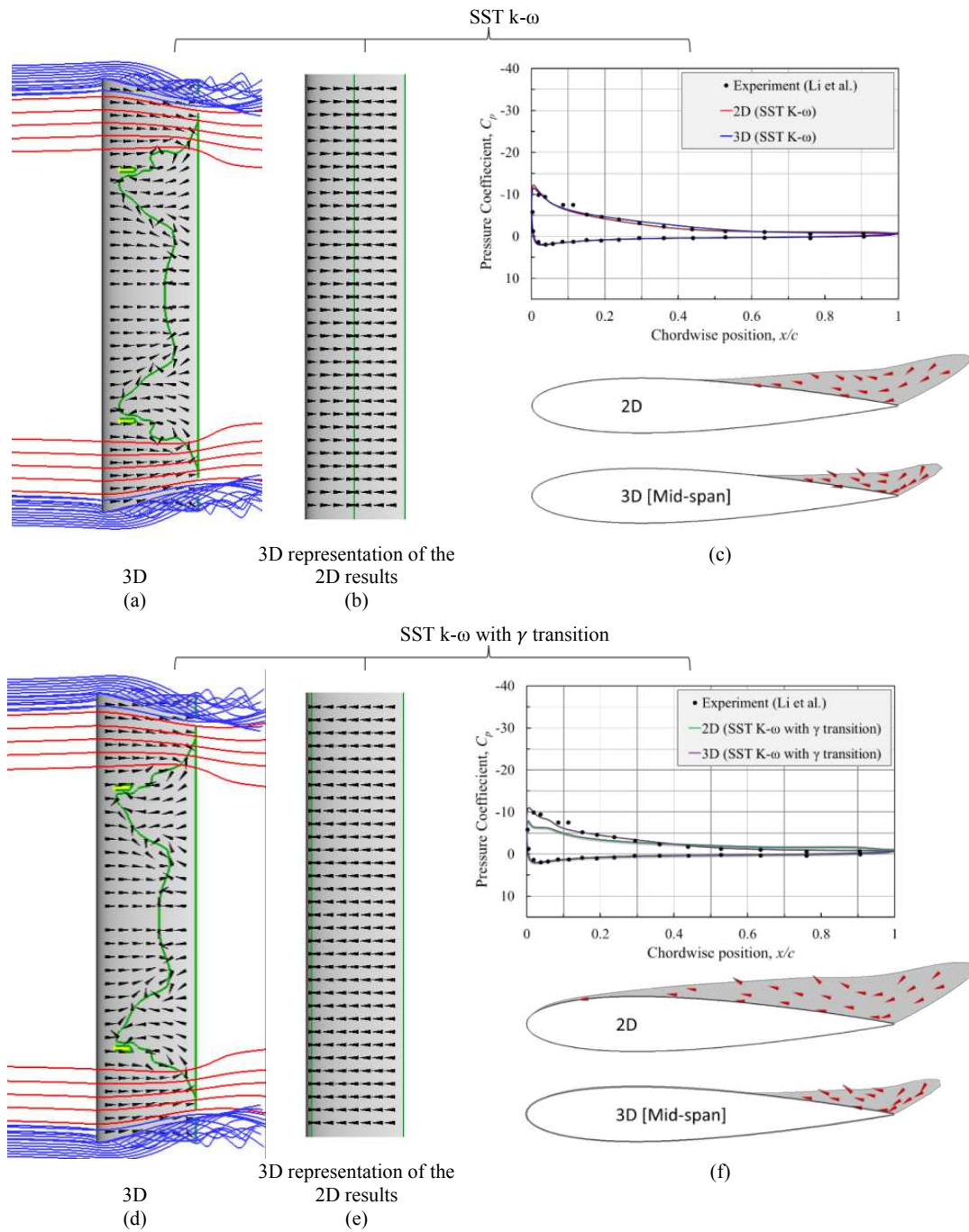

Figure 21 Comparisons between the 2D and 3D predictions at ϕ=150° including: (a, b, d, e) the flow pattern on the suction side, (c, f) the pressure coefficients and visualizations of the reverse flow region.

Figure 22 Comparisons between the 2D and 3D predictions at ϕ=240° including: (a, b, d, e) the flow pattern on the suction side, (c, f) the pressure coefficients and visualizations of the reverse flow region.
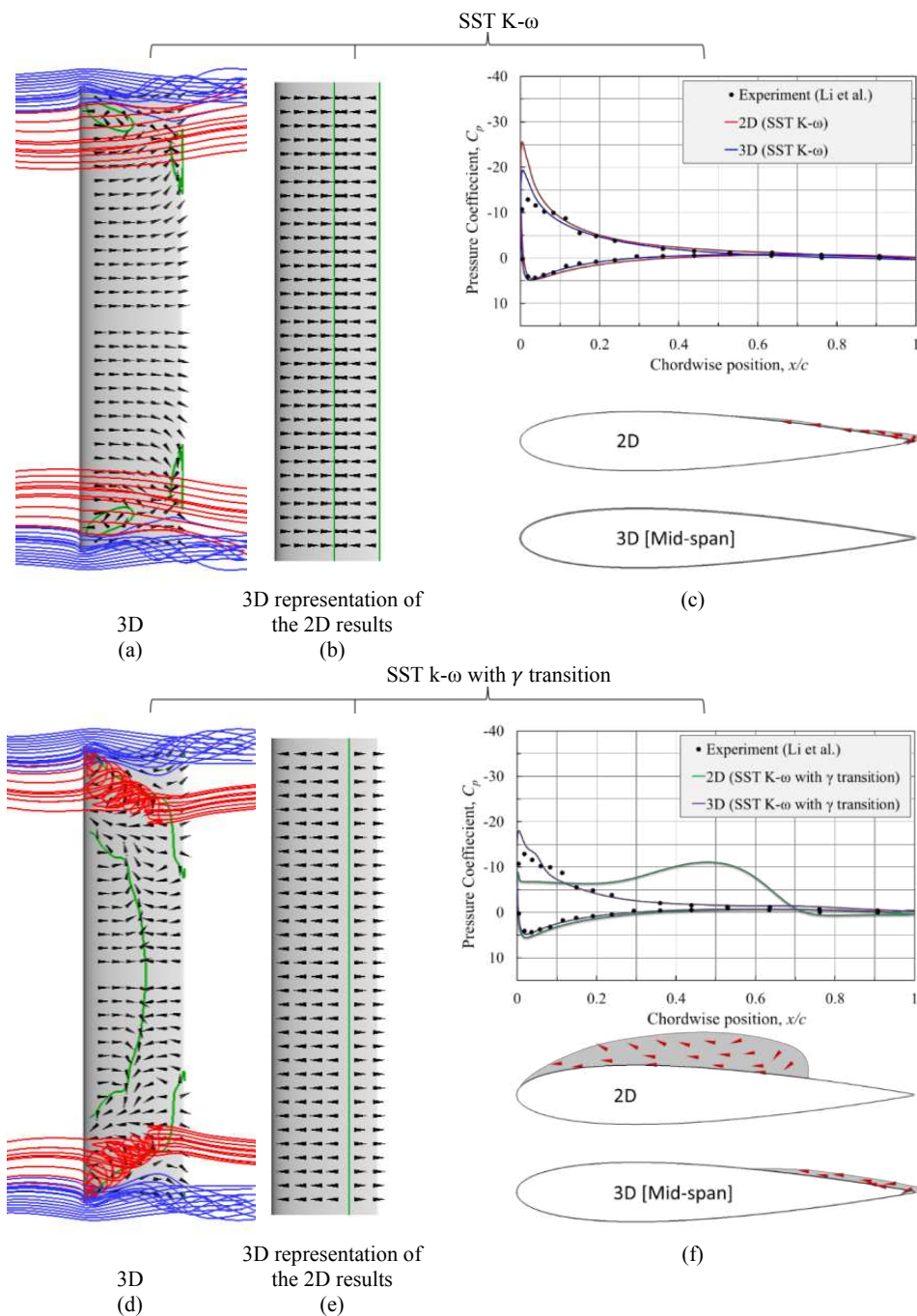
It is concluded that the results based on the SST k-ω with the γ transition turbulence model have large and unphysical separation in the 2D case at ϕ=240°. In the 3D case, the results based on the SST k-ω with the γ transition turbulence model shows a reverse flow zone at the mid-span section over the suction side at the normalized chordwise locations between x/c=0.6 and x/c=1, as shown in Figure 22 (f), while there is no reverse flow in the case of the SST k-ω turbulence, as shown in Figure 22 (c). However, it is observed in Figure 22 (f) that the pressure coefficient distribution has a slight deviation from the experimental data at the normalized chordwise locations between x/c=0.44 and x/c=0.91 in the 3D case based on the SST k-ω with the γ transition turbulence. This deviation is not

observed in the 3D case based on the SST k-ω turbulence. This suggests that the 3D results based on the SST k-ω turbulence have a better prediction of the flow pattern at the mid-span section at ϕ=240° in contrast with the results based on the SST k-ω with the γ transition turbulence.

In order to assess the 3D CFD predictions along the blade span, the predicted torque contributions at different spanwise sections are compared to the corresponding experimental data as shown in Figure 23. These spanwise locations include 70% of the blade half span, 80% of the blade half span, and the mid-span. These are referred to as z=0.70*h/2, z=0.80*h/2, and z=0.0, respectively, where z is the principle coordinate in the spanwise direction and h is the blade half span. It is observed

that the differences between the CFD predictions and the experimental data are relatively larger at z=0.70*h/2 and z=0.80*h/2 in contrast with the differences at the mid-span. This could be partially due to the simplified geometry of the supporting arms in the CFD model. It is observed in Figure 23 that the differences between the predictions based on the two turbulence models are minimal in the upstream part of the cycle, while there are considerable differences in the downstream part of the cycle at z=0.70*h/2 and z=0.80*h/2 in the region between ϕ=210° and ϕ=300°. In this region, the trend of predicted results based on the SST k-ω with the γ transition turbulence deviates from the trend of the experimental data. This suggests that the use of the SST k-ω turbulence is more suitable in the 3D case under the current setup, in contrast with the SST k-ω with the γ transition turbulence.

In order to perform quantitative comparisons between the CFD predictions and the experimental data, different quantitative parameters are chosen. These include the values of the average torque coefficient, $\bar{C}_m$, averaged over the whole cycle in addition to the upstream and downstream parts of the cycle. In addition, the maximum value of the torque coefficient, $\hat{C}_m$ is considered along with the azimuthal location of the maximum torque coefficient, ϕ at $\hat{C}_m$. Table 6 shows the quantitative comparisons between the predicted single blade values and the corresponding experimental data. It is observed that both the 2D and 3D predictions at the mid-span section have good agreements with the experimental data in the upstream part of the cycle. However, there are relatively large discrepancies in the CFD predictions in the downstream part of the cycle. In contrast with the mid-span section, the

deviation between the predicted and experimental values of the average torque coefficient is relatively larger at the other spanwise locations, i.e. z=0.70*h/2 and z=0.80*h/2.
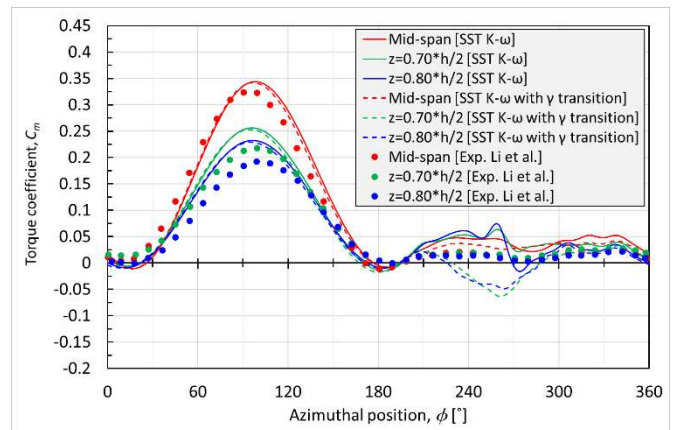

Figure 23 A comparison between the experimental data, 2D and 3D CFD results of torque coefficient at the different spanwise locations.

The predicted values of the maximum torque and its azimuthal location show a good agreement with the experimental data at the different spanwise locations. It is concluded that the main source of the quantitative differences between the CFD predictions and the experimental data are from the downstream part of the cycle that is associated with strong wake interactions. More detailed experimental data are needed in order to justify the source of these differences and whether the source is from numerical inefficiency or conceptual modelling errors.

Table 6 A comparison between the predicted and experimental values of the single blade average torque coefficient, $\bar{C}_m$, the maximum single blade torque coefficient, $\hat{C}_m$, and the azimuthal location of maximum torque coefficient, ϕ at $\hat{C}_m$ at different spanwise locations including: the mid-span, z=0.70*h/2, and z=0.80*h/2.

| | | | $\bar{C}_m$ | | | $\hat{C}_m$ | ϕ at $\hat{C}_m$ |
			Upstream part	Downstream part	Cycle-average		
Mid-span	Exp. (Li et al.)		0.151	0.013	0.082	0.325	93°
	2D CFD	SST k-ω	0.154	0.05	0.102	0.367	101.3°
		SST k-ω with γ transition	0.142	-0.004	0.069	0.358	99.3°
	3D CFD	SST k-ω	0.155	0.033	0.094	0.344	98.7°
		SST k-ω with γ transition	0.153	0.029	0.091	0.343	96°
z=0.70*h/2	Exp. (Li et al.)		0.108	0.018	0.063	0.218	99.3°
	3D CFD	SST k-ω	0.114	0.032	0.073	0.257	95.3°
		SST k-ω with γ transition	0.112	-0.0007	0.056	0.253	94.7°
z=0.80*h/2	Exp. (Li et al.)		0.091	0.013	0.052	0.192	99°
	3D CFD	SST k-ω	0.105	0.027	0.066	0.232	96.7°
		SST k-ω with γ transition	0.103	-0.001	0.051	0.229	94.7°

6. Conclusions

This paper investigates the best modelling strategy for VAWTs based on both the 2D and 3D CFD simulations. The two most highly employed turbulence models, namely the SST k-ω model and the SST k-ω with the γ transition model, are considered in this investigation. The novelty of this investigation is in the kind of data that is used in the validations of the CFD predictions. While most of the studies in the literature rely on some integral data, this investigation assesses the CFD predictions against a detailed instantaneous pressure data captured by a high-frequency pressure scanner. This provides a much better judgment on the behaviour of the CFD predictions based on the selected turbulence models. This paper sheds new light on how the behaviour of the predictions of the SST K-ω with the γ intermittency transition model changes between the 2D and 3D cases and how the trends of the 2D results based on this transition model deviates from the detailed experimental data. This behaviour has not been addressed before in the literature and this paper presents the first in-depth discussion on how this behaviour differs between the 2D and 3D cases. In contrast with the transitional version with the γ transition equation, the CFD predictions of both the instantaneous torque coefficient and the pressure coefficient around the blade based on the SST k-ω turbulence model have a much better agreement with the experimental data. Hence, we conclude that the SST k-ω turbulence model is recommended for both the 2D and 3D analyses under the current setup and operating conditions.

Acknowledgement

References

[1] International Energy Agency, "World Energy Outlook-Executive Summary," Paris, France, 2018.

[2] W. Tong, Wind power generation and wind turbine design. WIT Press publisher, 2010.

[3] S. Salah, E. C. H. Charqaouy, D. Saifaoui, O. Benzohra and A. Lebsir, "Integration of Decentralized Generations into the Distribution Network- Smart Grid Downstream of the Meter," International Journal of Smart Grid - ijSmartGrid, vol. 4, no. 1, 2020.

[4] Y. E. A. Eldahab and N. H. Saad, "Assessing Wind Energy Conversion Systems Based on Newly Developed Wind Turbine Emulator .," International Journal of Smart Grid - ijSmartGrid, vol. 4, no. 4, 2020.

[5] S. Ruiz and J. Espinosa, "Multi-objective optimal sizing design of a Diesel-PV-Wind-Battery hybrid power system in Colombia," International Journal of Smart Grid - ijSmartGrid, vol. 2, no. 1, March, pp. 49–57, 2018.

[6] K. Okedu, "A Variable Speed Wind Turbine Flywheel Based Coordinated Control System for Enhancing Grid Frequency Dynamics," International Journal of Smart Grids, ijSmartGrid, vol. 2, no. 2, 2018.

[7] D. M. Ramos and C. D. Sauceda, "CFD study of a vertical axis counter-rotating wind turbine," in 6th International Conference on Renewable Energy Research and Applications (ICRERA), 2017, vol. 5, pp. 240–244.

[8] F. Balduzzi, A. Bianchini, E. A. Carnevale, L. Ferrari and S. Magnani, "Feasibility analysis of a Darrieus vertical-axis wind turbine installation in the rooftop of a building," Applied Energy, vol. 97, pp. 921–929, 2012.

[9] A. Bianchini, F. Balduzzi, P. Bachant, G. Ferrara and L. Ferrari, "Effectiveness of two-dimensional CFD simulations for Darrieus VAWTs: a combined numerical and experimental assessment," Energy Conversion and Management, vol. 136, pp. 318–328, Mar. 2017.

[10] L. Battisti, E. Benini, A. Brighenti, S. Dell'Anna and M. Raciti Castelli, "Small wind turbine effectiveness in the urban environment," Renewable Energy, vol. 129, pp. 102–113, 2018.

[11] M. M. Elsakka, D. B. Ingham, L. Ma and M. Pourkashanian, "CFD analysis of the angle of attack for a vertical axis wind turbine blade," Energy Conversion and Management, vol. 182, pp. 154–165, 2019.

[12] T. T. Zhang, M. Elsakka, W. Huang, Z. G. Wang, D. B. Ingham, L. Ma, and M. Pourkashanian, "Winglet design for vertical axis wind turbines based on a design of experiment and CFD approach," Energy Conversion and Management, vol. 195, pp. 712–726, 2019.

[13] N. Rosado Hau, L. Ma, D. Ingham and M. Pourkashanian, "A critical analysis of the stall onset in vertical axis wind turbines," Journal of Wind Engineering and Industrial Aerodynamics, vol. 204, p. 104264, Sep. 2020.

[14] M. H. Mohamed, A. Dessoky and F. Alqurashi, "Blade shape effect on the behavior of the H-rotor Darrieus wind turbine: Performance investigation and force analysis," Energy, vol. 179, pp. 1217–1234, Jul. 2019.

[15] M. M. Elsakka, D. B. Ingham, L. Ma and M. Pourkashanian, "Effects of turbulence modelling on the predictions of the pressure distribution around the wing of a small scale vertical axis wind turbine," in Proceedings of the 6th European Conference on Computational Mechanics: Solids, Structures and Coupled Problems, ECCM 2018 and 7th European Conference on Computational Fluid Dynamics, ECFD 2018, 2020, pp. 3921–3931.

[16] Y. Celik, L. Ma, D. Ingham and M. Pourkashanian, "Aerodynamic investigation of the start-up process of H-type vertical axis wind turbines using CFD," Journal of Wind Engineering and Industrial

Aerodynamics, vol. 204, p. 104252, Sep. 2020.

[17] I. Paraschivoiu, "Double-multiple streamtube model for Darrieus in turbines," in Proceedings of the 2nd DOE/NASA wind turbines dynamics workshop, 1981.

[18] A. M. Biadgo, A. Simonovic, D. Komarov and S. Stupar, "Numerical and Analytical Investigation of Vertical Axis Wind Turbine," FME Transactions, vol. 41, pp. 49–58, 2013.

[19] N. Rosado Hau, L. Ma, D. Ingham and M. Pourkashanian, "A Procedure to Predict the Power Coefficient of Vertical Axis Wind Turbines at Low Tip Speed Ratios," in AIAA Scitech 2019 Forum, 2019.

[20] J. H. Strickland, B. T. Webster and T. Nguyen, "A Vortex Model of the Darrieus Turbine: An Analytical and Experimental Study," Journal of Fluids Engineering, vol. 101, no. 4, pp. 500–505, 1979.

[21] E. Dyachuk and A. Goude, "Numerical Validation of a Vortex Model against ExperimentalData on a Straight-Bladed Vertical Axis Wind Turbine," Energies, vol. 8, no. 10, pp. 11800–11820, 2015.

[22] M. Ghasemian, Z. N. Ashrafi and A. Sedaghat, "A review on computational fluid dynamic simulation techniques for Darrieus vertical axis wind turbines," Energy Conversion and Management, vol. 149, pp. 87–100, Oct. 2017.

[23] H. Day, D. Ingham, L. Ma and M. Pourkashanian, "Adjoint based optimisation for efficient VAWT blade aerodynamics using CFD," Journal of Wind Engineering and Industrial Aerodynamics, vol. 208, pp. 1–17, 2021.

[24] X. Jin, G. Zhao, K. Gao and W. Ju, "Darrieus vertical axis wind turbine: Basic research methods," Renewable and Sustainable Energy Reviews, vol. 42, pp. 212–225, 2015.

[25] B. Paillard, J.-A. Astolfi and F. Hauville, "CFD simulation and experimental validation of a vertical axis turbine: toward variable pitch cross-flow marine turbine for maximizing hydropower extraction—the SHIVA project," in Volume 5: Ocean Space Utilization; Ocean Renewable Energy, 2011, pp. 619–627.

[26] R. Firdaus, T. Kiwata, T. Kono and K. Nagao, "Numerical and experimental studies of a small vertical-axis wind turbine with variable-pitch straight blades," Journal of Fluid Science and Technology, vol. 10, no. 1, pp. 1–15, 2015.

[27] R. Howell, N. Qin, J. Edwards and N. Durrani, "Wind tunnel and numerical study of a small vertical axis wind turbine," Renewable Energy, vol. 35, no. 2, pp. 412–422, Feb. 2010.

[28] M. S. Siddiqui, N. Durrani and I. Akhtar, "Quantification of the effects of geometric approximations on the performance of a vertical axis wind turbine," Renewable Energy, vol. 74, pp. 661–670, 2015.

[29] N. Franchina, G. Persico and M. Savini, "2D-3D Computations of a Vertical Axis Wind Turbine Flow Field: Modeling Issues and Physical Interpretations," Renewable Energy, pp. 1170–1189, 2019.

[30] A. Rezaeiha, H. Montazeri and B. Blocken, "On the accuracy of turbulence models for CFD simulations of vertical axis wind turbines," Energy, vol. 180, pp. 838–857, 2019.

[31] K. M. Almohammadi, D. B. Ingham, L. Ma and M. Pourkashanian, "Modeling dynamic stall of a straight blade vertical axis wind turbine," Journal of Fluids and Structures, vol. 57, pp. 144–158, 2015.

[32] L. Daróczy, G. Janiga, K. Petrasch, M. Webner and D. Thévenin, "Comparative analysis of turbulence models for the aerodynamic simulation of H-Darrieus rotors," Energy, vol. 90, pp. 680–690, 2015.

[33] J. Chaiyanupong and T. Chitsomboon, "Effects of turbulence models and grid densities on computational accuracy of flows over a vertical axis wind turbine," International Journal of Renewable Energy Development, vol. 7, no. 3, pp. 213–222, 2018.

[34] J. McNaughton, F. Billard and A. Revell, "Turbulence modelling of low Reynolds number flow effects around a vertical axis turbine at a range of tip-speed ratios," Journal of Fluids and Structures, vol. 47, pp. 124–138, 2014.

[35] K. Rogowski, "Numerical studies on two turbulence models and a laminar model for aerodynamics of a vertical-axis wind turbine," Journal of Mechanical Science and Technology, vol. 32, no. 5, pp. 2079–2088, 2018.

[36] Q. Li, T. Maeda, Y. Kamada, J. Murata, T. Kawabata, K. Shimizu, T. Ogasawara, A. Nakai, T. Kasuya, "Wind tunnel and numerical study of a straight-bladed vertical axis wind turbine in three-dimensional analysis (Part I: For predicting aerodynamic loads and performance)," Energy, vol. 106, pp. 443–452, 2016.

[37] ANSYS Inc., "ANSYS FLUENT Theory Guide," Canonsburg, 2013.

[38] ANSYS Inc., "ANSYS FLUENT User's Guide," Canonsburg, 2013.

[39] A. Rezaeiha, H. Montazeri and B. Blocken, "Towards accurate CFD simulations of vertical axis wind turbines at different tip speed ratios and solidities: Guidelines for azimuthal increment, domain size and convergence," Energy Conversion and Management, vol. 156, pp. 301–316, Jan. 2018.

[40] ANSYS Inc., "ANSYS Meshing User's Guide," Canonsburg, 2010.

[41] ANSYS Inc., "ANSYS CFD-Post User's Guide," Canonsburg, 2017.